

Laboratory Report

Rohit Kumar Bajaj 34491147

Abstract

This report examines the aerodynamic performance of a NACA 0020 airfoil for a UAV designed for forest fire mapping, addressing the challenge of optimizing lift and drag for operational efficiency. The study investigates 2D and 3D aerodynamic effects, comparing experimental, computational (CFD), and theoretical predictions. Methodologies included wind tunnel tests, boundary layer measurements, and airfoil section analysis to evaluate pressure distribution, lift, and drag characteristics. Key outputs were pressure plots, lift curve slope plots, boundary layer profiles, and C_L and C_D plots, which helped assess the wing's aerodynamic efficiency. The findings validate aerodynamic models, highlight experimental errors and the limitations of numerical tools due to inherent assumptions, and collectively support the optimization of the UAV wing for real-world applications.

Keywords

Uncertainty — Experimental Analysis — Theoretical Analysis

1. Introduction

The aerodynamic analysis of a wing is essential to optimize performance and meet operational demands. This study investigates the aerodynamic characteristics of a wing with a NACA 0020 airfoil, a chord length of 0.4 m, and a span of 2.2 m, focusing on lift and drag properties using theoretical, computational, and experimental approaches.

The analysis incorporates flat plate theory to model boundary layer properties and viscous drag, followed by airfoil testing to evaluate pressure distribution and lift coefficients at various angles of attack. Results from CFD simulations, XFOIL analysis, and wind tunnel experiments are compared to validate predictions. Finite wing effects, such as induced drag and tip vortex formation, are analyzed using wind tunnel data and numerical simulation tools like XFLR5, providing a comprehensive assessment of the wing's aerodynamic performance and insights into deviations and trends for similar systems.

2. Methods

The analysis in this report draws from five primary sources: an infinite-wing laboratory, a finite-wing laboratory, a boundary layer laboratory, computational fluid dynamics (CFD) simulations, and XFLR5, providing a comprehensive evaluation of aerodynamic theory.

2.1 CFD

The CFD analysis for the 2D wing was conducted to evaluate aerodynamic performance, focusing on pressure distribution, velocity gradients, streamlines, and the mesh definition. The flow problem was defined using the $k-\varepsilon$ turbulence model, with geometry and operating conditions at the inlet and outlet modeled in a computational domain for varying angles of attack. A structured, high-quality mesh was generated as shown by Figure 1(b). Mesh refinement using cell registers was used to improve accuracy, especially near critical regions such as the leading edge, trailing edge, and transition point, where flow behavior is highly sensitive.

Key outputs, including lift and drag coefficients, pressure contours, velocity vectors, and streamlines, were extracted (Figures 1(a), 1(c), and 1(d)). The pressure contours highlighted high and low-pressure

regions across the airfoil, while velocity vectors revealed flow separation and recirculation zones.

Additionally, streamlines plotted at a 14° angle of attack (Figure 1(d)) provided visual confirmation of aerodynamic performance at higher angles of attack and were instrumental in identifying the onset and extent of flow separation.

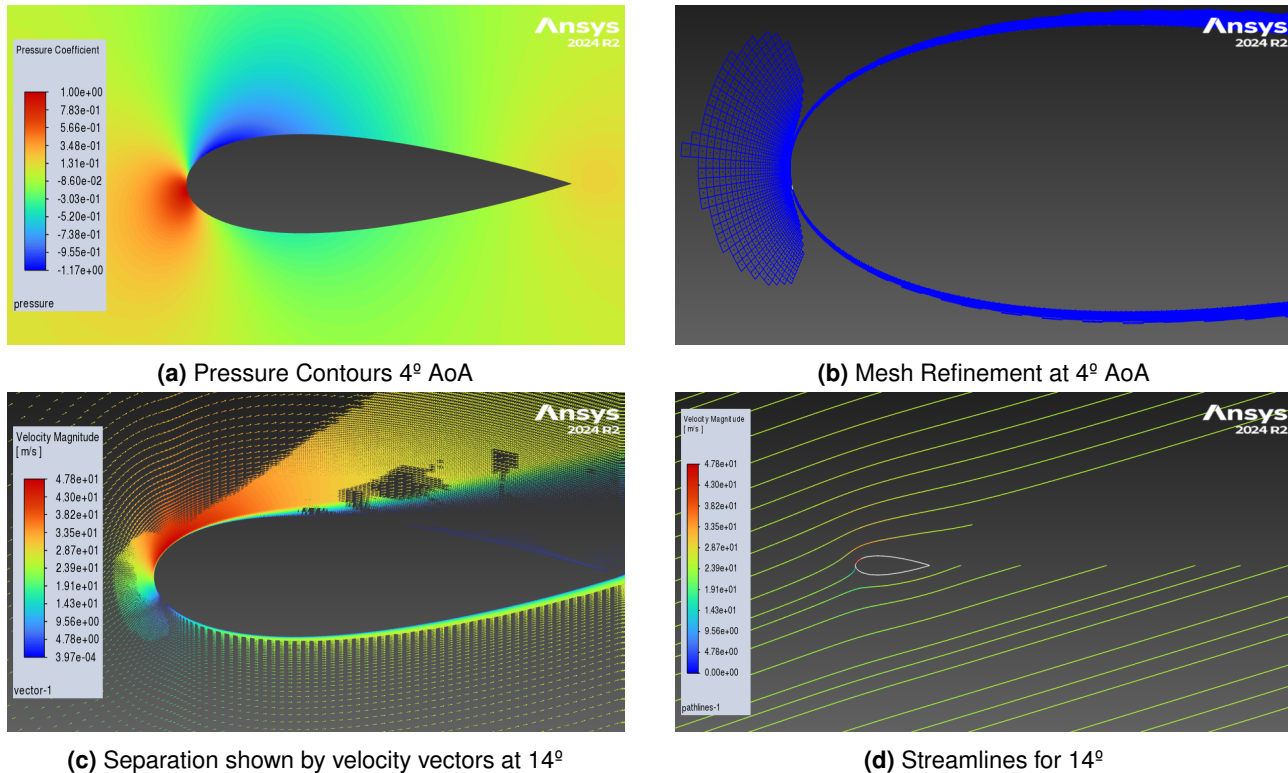


Figure 1. CFD Analysis for different angles of attack

2.2 Boundary Layer Lab

The boundary layer experiment examined velocity profiles and properties over a flat plate at various Reynolds numbers. Conducted in a low-speed wind tunnel, the setup featured a flat plate with smooth and rough sides and a Pitot tube (1 mm tip) to measure velocity via pressure. The setup is shown in Figure 2 [3]. A micrometer allowed precise positioning of the tube to construct velocity profiles and calculate boundary layer thickness and velocity gradients. Multiple freestream velocities were tested to evaluate how the Reynolds number affected boundary layer characteristics.

Key errors included potential damage to the fragile Pitot tube, missed near-wall data from quick movements, and user inaccuracies in micrometer readings. The Pitot tube's averaging nature also limited its ability to capture flow fluctuations. Despite these challenges, careful handling yielded reliable data and insights into boundary layer behavior.



Figure 2. Wind tunnel and Pitot tube setup.

2.3 Airfoil Lab

The airfoil lab investigates the pressure distribution around an infinite-span aerofoil, the effects of varying angles of attack, and the resulting lift. The aerofoil spans the wind tunnel's working section to maintain two-dimensional flow, where the flow never reaches the tips (Figure 3a). Twelve 2.5 mm pressure tappings, linked to a multi-manometer (Figure 3b), measure static pressure at various points. A pitot-static probe at the inlet measures stagnation and freestream static pressures for calculating pressure coefficients, lift, and pressure drag.

Each participant tested three angles of attack, with group results averaged to minimize uncertainty. The multi-manometer highlights pressure differences between the aerofoil's suction and pressure sides, shown by higher pressure on the left (pressure side) and lower pressure on the right (suction side). Unclean tubes affected meniscus visibility, impacting accuracy. An uncertainty check, such as verifying the zero-lift angle of the symmetric NACA 0020 airfoil (theoretically zero), helps detect setup or data errors [4].

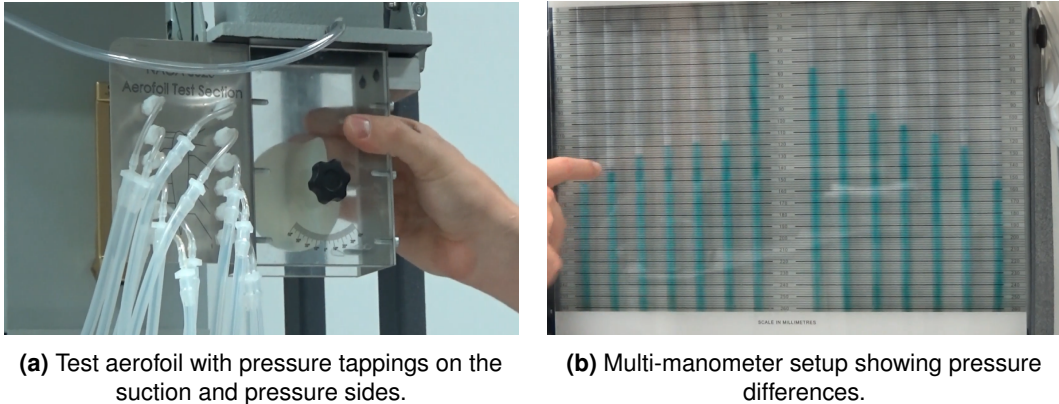


Figure 3. Visualization of the experimental setup for the airfoil lab.

2.4 Finite Wing Lab

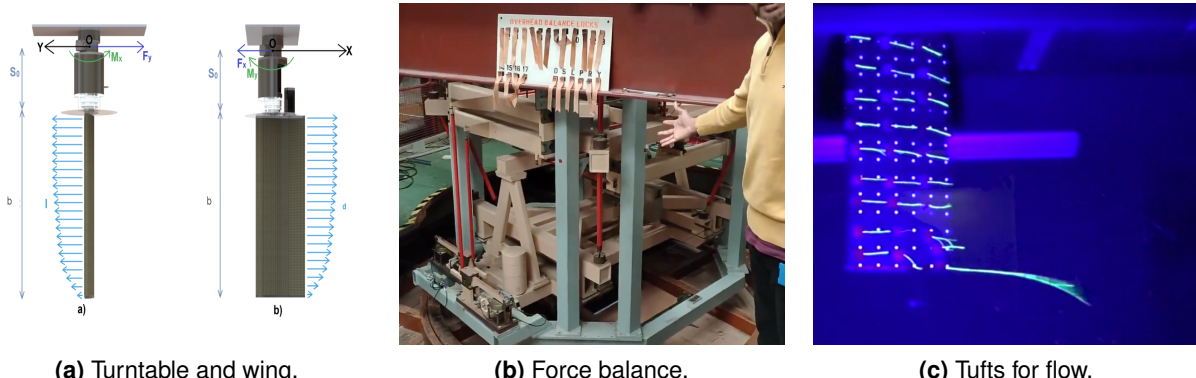


Figure 4. Experimental setup and tools: (a) turntable with mounted wing, (b) overhead force balance schematic, and (c) tufts for visualizing attached and separated flow.

Finite-wing experiments were conducted in the R.J. Mitchell Wind Tunnel, a closed-circuit, recirculating facility with an 11x8 ft test section and a maximum freestream velocity of 40 m/s, supporting applications from Formula 1 to ship hull testing. Tests used a rectangular wing with a NACA 0020 cross-section, a 0.4 m chord, and a 1.11 m half-span, at a freestream velocity of 20 m/s.

A fixed 6-axis force/moment balance (Figure 4b) measured aerodynamic forces and moments, capturing critical chord-wise and normal forces (Figure 4a). The wing, mounted on a turntable, allowed angle-of-attack adjustments while the balance rotated with it. The testing was carried out from -20 to 4° AoA allowing us to see the suction side and how the stall cell grew. Tufts on the wing surface (Figure 4c) visualized flow, with straight tufts indicating attached flow at lower angles of attack and oscillating tufts signaling separation at larger angles of attack. The force balance's ± 0.05 N uncertainty is significant for low-force data, requiring careful analysis of aerodynamic trends

3. Results and Discussions

Lift measurements for a NACA0020 aerofoil (2D) were obtained and compared with CFD results and XFOIL to evaluate accuracy. 3D wing lift performance was analyzed using wind tunnel data and compared with XFLR5 simulations to assess numerical and experimental consistency.

3.1 Measuring and Predicting Lift

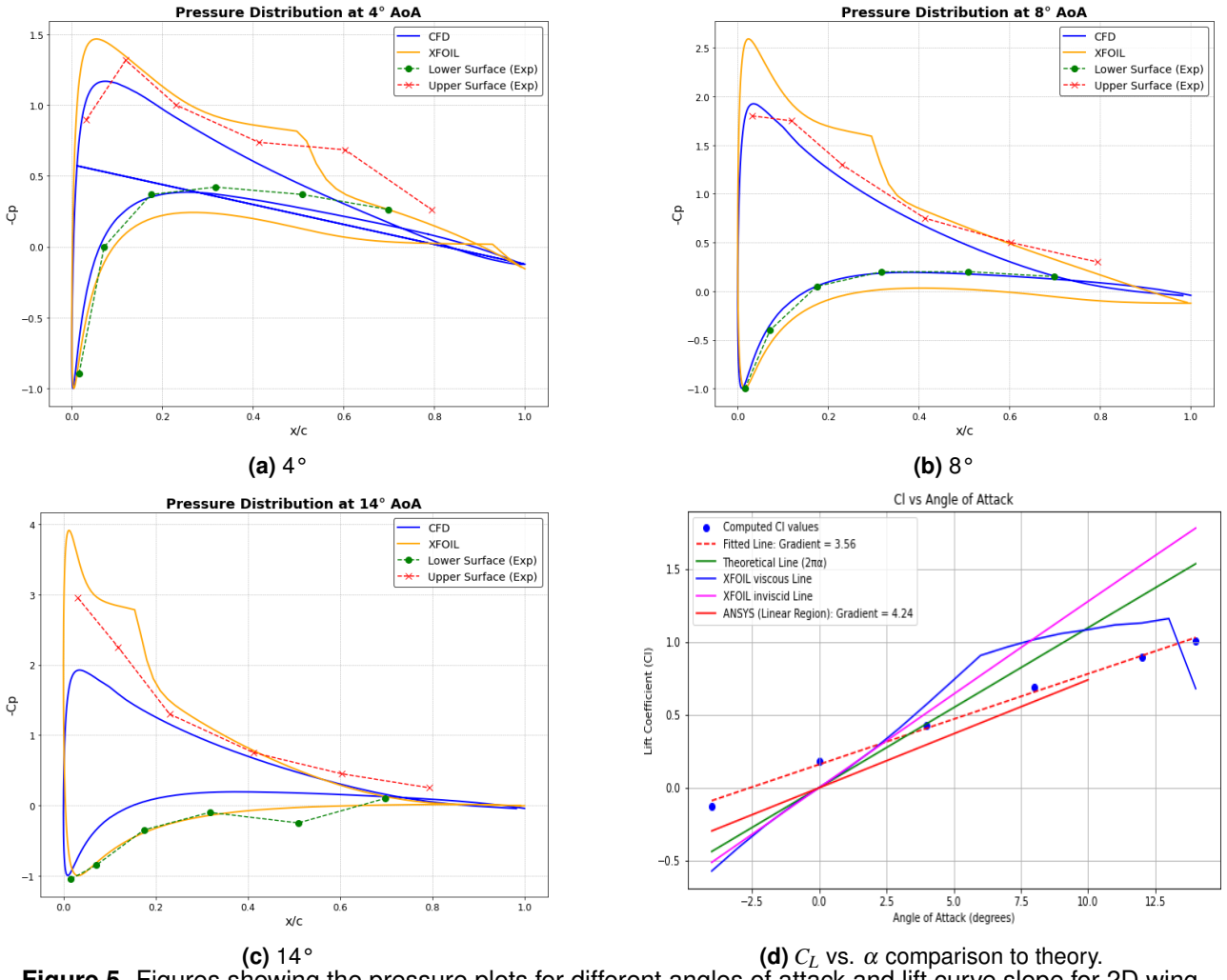


Figure 5. Figures showing the pressure plots for different angles of attack and lift curve slope for 2D wing.

For the infinite wing the pressure coefficient was derived using Bernoulli's equation, with readings resolved tangentially and normally to the airfoil surface and numerically integrating as per equations (1.2) and (1.3).

$$C_N = \frac{N}{\frac{1}{2}\rho u_\infty^2 c} = \frac{1}{c} \int_0^c (C_{p,u} - C_{p,l}) dx \quad (1.1) \quad C_T = \frac{T}{\frac{1}{2}\rho u_\infty^2 c} = \frac{1}{c} \int_0^c \left(C_{p,u} \frac{dy_u}{dx} - C_{p,l} \frac{dy_l}{dx} \right) dx \quad (1.2)$$

Figure 5 compares pressure distributions and lift trends at various angles of attack. At 4° and 8°, experimental results align closely with CFD, while XFOIL shows deviations due to its idealized assumptions, such as inviscid flow, viscous-inviscid coupling, and simplified boundary layer transition modeling. XFOIL overestimates suction pressure, particularly at higher angles, as it may fail to account for the effect of high adverse pressure gradients, which in reality reduce the pressure peak due to turbulence and flow separation. At 14°, experimental results deviate significantly from both CFD and XFOIL. While CFD provides more realistic predictions by solving the Navier-Stokes equations and partially accounting for turbulence, it may not fully capture surface roughness and experimental uncertainties. However, XFOIL matches more closely with the lower surface experimental data because the flow there is predominantly attached and laminar, aligning well with XFOIL's boundary layer solver. [1].

After the integration and using trigonometry, the lift coefficient is computed as:

$$C_L = C_N \cos(\alpha) - C_T \sin(\alpha) \quad (2)$$

Figure 5(d) compares C_L versus α for the NACA 0020 airfoil, showing experimental, CFD, XFOIL (viscous/inviscid), and theoretical predictions. All lines correctly show zero lift at zero angle of attack, consistent with the symmetry of the airfoil. The theoretical slope of 2π assumes inviscid, incompressible, and steady potential flow, which partially applies in idealized conditions but not in experiments, where there is a 76% difference in gradient between theory and experimental results.

XFOIL's viscous line initially overpredicts lift compared to experiments but aligns more closely as α increases, with its slope factor approximately matching the experimental trend until around 12 degrees. Beyond this point, it fails to model flow separation accurately. By comparison, CFD results show only a 19% difference in gradient from the experimental data, as CFD better accounts for turbulence and viscous effects. However, even CFD cannot fully capture surface roughness or wind tunnel imperfections, highlighting the limitations of both numerical and theoretical models under real-world conditions.

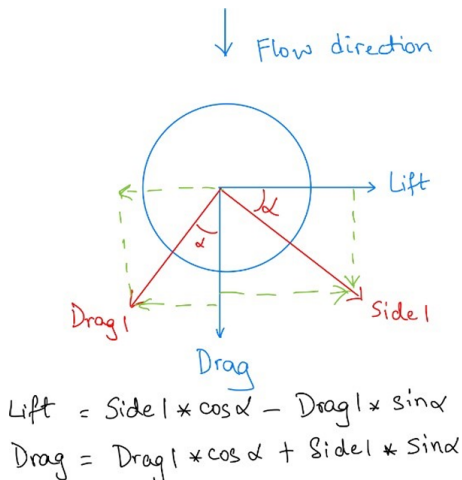
Finite wing 3D effects were modeled using a turntable and overhead balance system in the RJ Mitchell Wind Tunnel. Forces were resolved to calculate C_L at varying α , as shown in Figure 6b, demonstrating how C_L changes with α [2].

The experimental lift slope ($a = 3.754$) is lower than the XFLR5 value ($a = 4.34$) due to differences in modeling assumptions and physical phenomena. XFLR5, based on potential flow theory, assumes inviscid, incompressible conditions and neglects viscous effects and flow separation. Additionally, XFLR5 uses flat quad panels to approximate the 3D wing geometry, which oversimplifies the true curvature of the wing [1]. This simplification can lead to an overestimation of lift, especially at higher angles of attack, as the model perceives less curvature than exists, thereby underestimating adverse effects like flow separation. Experimental data, on the other hand, accounts for real-world phenomena such as viscous drag, boundary layer development, and finite span-induced drag, which collectively result in a shallower lift slope compared to the XFLR5 predictions.

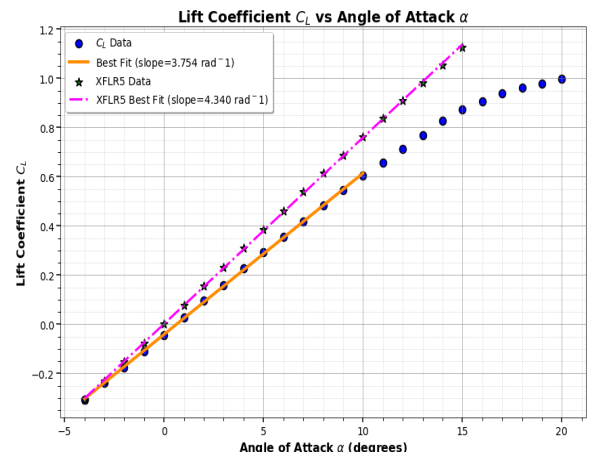
$$a = \frac{a_0}{1 + \frac{a_0}{\pi AR}(1 + \tau)} \quad (3.1)$$

$$a = \frac{a_0}{\sqrt{1 + \left(\frac{a_0}{\pi AR}\right)^2} + \frac{a_0}{\pi AR}} \quad (3.2)$$

A negative $\tau = -1.0633$ was obtained from Equation (3.1), which is unphysical as it implies an impossible improvement in lift slope. This likely arose from using half the wing span in the experiment. Using Helmbold's formula (Equation 3.2) with $AR = 2.4$ (calculated as $AR = \frac{(\text{half span})^2}{\text{area of half span}}$), the corrected lift curve slope $a = 4.1$ matches XFLR5 and experimental results, validating the formula. XFLR5 gave a tau of 0.6 which somewhat aligns with theory.



(a) Resolved lift and drag



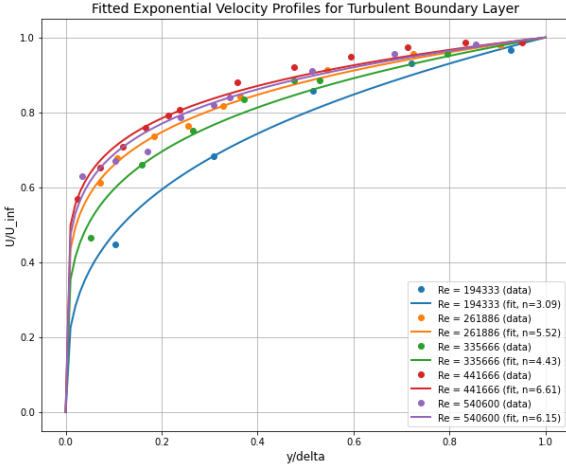
(b) Lift curve slope plot for 3D wing

Figure 6. Figures including 3D lift curve slope and resolved forces for lift and drag.

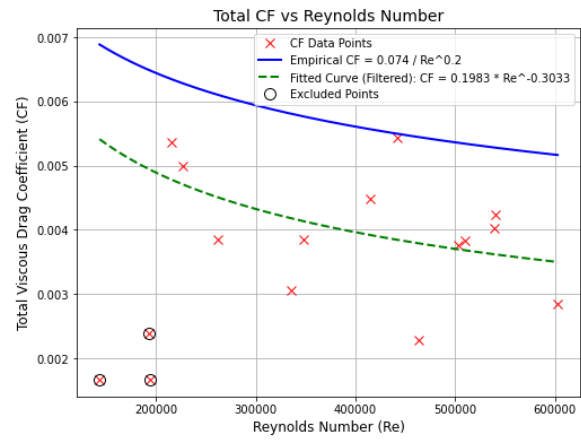
3.2 Measuring and Predicting Drag

This section analyzes boundary layer properties over a flat plate to estimate viscous drag and compare results with theoretical predictions. Momentum thickness (θ) and the viscous drag coefficient (C_F) were experimentally determined, and a power-law curve was fitted to establish a predictive relationship regarding the viscous drag component of C_{D_0} .

In the experiment, velocity profiles were recorded near the trailing edge of the flat plate, positioned 265 mm from the leading edge. A pitot probe was traversed across the boundary layer to measure velocity, later enabling the calculation of boundary layer parameters (δ , δ^* , and θ) and their relationship to the Reynolds number (Re_L).



(a) Velocity profile for different Reynolds number



(b) Power-law form for a turbulent boundary layer

Figure 7. Figures including velocity profiles for boundary layer.

Boundary layers can be laminar or turbulent, strongly influenced by the Reynolds number. At high Reynolds numbers, as observed in the experiment, the boundary layer transitions to turbulence, exhibiting enhanced mixing due to chaotic eddies. This mixing increases momentum transfer between fluid layers, sharpening the velocity gradient near the wall and resulting in thinner boundary layers (δ).

In Figure 7a, sharper velocity profiles at higher Reynolds numbers indicate stronger mixing [5], with steeper gradients near the wall signifying increased shear stress and drag. The rise in the power-law parameter n with Reynolds number, shown in the fitted curves, highlights stronger turbulent effects that steepen the velocity profile. The thinner boundary layer thickness (δ) at higher Re reflects greater momentum diffusion, confining the high-velocity region closer to the wall. The viscous drag coefficient C_F was calculated using the boundary layer properties, particularly the momentum thickness θ , determined by integrating the velocity profile:

$$\theta = \int_0^\infty \frac{u}{U_\infty} \left(1 - \frac{u}{U_\infty}\right) dy \quad (3)$$

$$C_F = 0.1983 \cdot Re^{-0.3033} \quad (3.1)$$

The presence of a turbulent boundary layer was confirmed by calculating the shape factor (H) using the displacement thickness (δ^*) and momentum thickness (θ). For Reynolds numbers $Re = 441,666$ and $Re = 261,886$, the shape factors were $H = 1.2814$ and $H = 1.2617$, respectively, both below 2, indicating it was turbulent.

This curve fit, shown in Figure 7b, provides a practical tool for estimating the viscous drag coefficient of the finite wing used in the experiment by substituting the corresponding Reynolds number. The deviation from the theoretical equation $C_F = \frac{0.074}{Re^{0.2}}$ can be attributed to several factors. Measurement uncertainties, such as errors in velocity profile acquisition and boundary layer property determination, could lead to discrepancies. The flat plate used can be modelled as a finite wing introducing three-

dimensional effects, such as spanwise flow and tip vortices, which alter boundary layer development compared to the assumptions for an infinite flat plate. Additionally, turbulence effects may vary at lower Reynolds numbers, where the boundary layer could be in a transitional state rather than fully turbulent, making the theoretical predictions less applicable. Excluding the lower Reynolds number data as shown in Figure 7b, minimizes the impact of these transitional effects and potential experimental noise, focusing on conditions where turbulence is well-developed and the empirical fit is more reliable.

The Finite Wing lab allowed the extraction of C_L and C_D , which were used in conjunction with the following drag polar equation:

$$C_D = C_{D0} + K \cdot C_L^2 \quad (4)$$

This equation separated the induced drag component, which arises due to the finite wing and the effect of tip vortices. The finite wing causes tip vortices that result in a component of the lift acting in the direction of the drag. Therefore, there is an additional drag due to lift contribution in the presence of the finite wing. This drag due to lift is also known as the *induced drag*.

The C_{D0} component is also known as the zero-lift drag coefficient, which denotes the drag experienced by the wing at zero lift. This total drag is typically comprised of the skin-friction drag, pressure drag and interference drag. The discrepancy between the experimental and theoretical viscous drag values can be attributed to several factors. One key reason is that the flow over the wing might be transitional rather than fully turbulent. The theoretical prediction assumes turbulent boundary layer flow, which tends to overpredict viscous drag when the actual flow is in a transitional regime. This transitional behavior could explain the lower experimental value of 1.912 compared to the theoretical value of 2.352 (as summarized in Table 2). Additionally, the scatter observed in the data points as shown earlier in Figure 7b indicates potential inconsistencies in the measurements. The data was collected from multiple group members, and possible post-processing errors in the experimental data could have compounded the overall experimental error.

Parameter	Value
Viscous drag (experimental relationship)	1.91
Viscous drag (theoretical prediction)	2.35
Total zero-lift drag	10.11
Difference	8.20

Table 1. Summary of Drag Parameters

In calculating the total zero-lift drag from the drag polar C_{D0} shown in Figure 8 , a value of 10.11 was obtained, from which the viscous drag was subtracted to determine the remaining drag components. This difference of 8.20 suggests the presence of other drag mechanisms beyond viscous drag. In particular, pressure drag or interference drag likely contribute to the total drag observed. Pressure drag can result from flow separation around the wing, while interference drag may arise due to the interaction between the wing and other components in the experimental setup. These forms of drag highlight the complexity of real-world aerodynamic flows compared to idealized theoretical predictions.

3.3 Overall performance of the wing

The wing's performance was analyzed by combining experimental data and computational results from XFLR5. The drag polar (Figure 8) demonstrates the relationship between the lift coefficient (C_L) and drag coefficient (C_D), providing insight into the aerodynamic efficiency of the wing as well as its drag characteristics.

The maximum glide ratio achieved was 10.42, occurring at an angle of attack (α) of 10°, as shown in Figure 8. This indicates the angle at which the wing operates most efficiently, offering the highest lift-to-drag ratio for optimal performance. XFLR5 overpredicts this glide ratio and says it will happen at lower angles of attack.

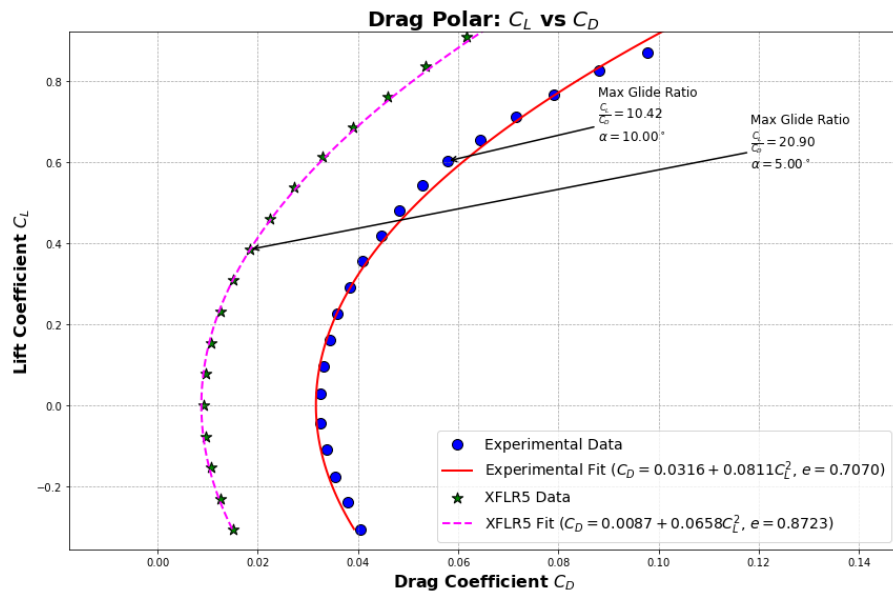


Figure 8. Drag polar including maximum glide ratio.

The Oswald efficiency factor (e) derived from the experimental data is 0.7070, slightly lower than the 0.8723 obtained from XFLR5. This discrepancy likely arises from differences in flow characteristics, including experimental uncertainties or simplifications in the XFLR5 model. XFLR5 appears to underestimate drag, which may be the viscous component, which may result from wind tunnel conditions not being as laminar as assumed, with transition perhaps occurring at some point along the chord. Notably, XFLR5 interpolates 2D results to estimate the viscous drag of the wing in 3D.

Despite these differences, the experimental fit follows a parabolic trend, consistent with theoretical expectations, and aligns well with XFLR5 predictions. This agreement validates the experimental methods while highlighting areas where computational models could be improved.

4. Conclusions

The objective of this lab - to predict and analyze the aerodynamic performance of the NACA 0020 airfoil—was achieved. The experimental results showed reasonable agreement with numerical predictions and theoretical models, with CFD predictions matching experimental data more closely than XFOIL or XFLR5 due to the incorporation of a viscous model. However, XFOIL and XFLR5 provided valuable insights into expected performance trends and facilitated comparisons with thin airfoil theory and potential flow theory, which align with their underlying assumptions.

For future work, improvements could include the use of more advanced sensors, such as scanivalve systems, which would be particularly beneficial for capturing detailed boundary layer behavior where instantaneous pressure is measured where a standard pitot tube might average readings. Additionally, incorporating transition effects in the XFLR5 analysis could enhance the agreement between numerical and experimental results. The use of the viscous module in XFOIL for infinite wing conditions proved useful and could be further refined for improved accuracy.

Overall, the lab demonstrated the value of combining experimental, computational, and theoretical approaches for evaluating aerodynamic performance and provided a comprehensive understanding of the NACA 0020 airfoil's behavior.

References

- [1] “Theoretical limitations and shortcomings of xflr5.” [Online]. Available: <https://www.xflr5.tech/docs/Part%20IV:%20Limitations.pdf>. [Accessed: Jan. 8, 2025].
- [2] SESX, “Finite Wing Lab and Processing Notebook,” Jupyter Notebook, 2024.
- [3] SESX, “Boundary Layer Lab,” Jupyter Notebook, 2024.
- [4] SESA/SESS, “Aerofoil Lab,” Jupyter Notebook, 2024.
- [5] “Laminar and Turbulent Boundary Layers,” Cam.ac.uk, 2019. http://www-mdp.eng.cam.ac.uk/web/library/enginfo/aerothermal_dvd_only/aero/fprops/introvisc/node8.html